The Astrophysical Journal Letters, 970:L36 (7pp), 2024 August 1 https://doi.org/10.3847/2041-8213/ad5fff

Evaluation of Scale-dependent Kurtosis with HelioSwarm

Francesco Pecora[1], Francesco Pucci[2], Francesco Malara[3], Kristopher G. Klein[4], Maria Federica Marcucci[5], Alessandro Retinò[6], and William Matthaeus[1]
[1] Department of Physics and Astronomy, University of Delaware, Newark, DE 19716, USA; fpecora@udel.edu
[2] Istituto per la Scienza e Tecnologia dei Plasmi, Consiglio Nazionale delle Ricerche (ISTP-CNR), 70126 Bari, Italy
[3] Dipartimento di Fisica, Università della Calabria, 87036 Rende CS, Italy
[4] Lunar and Planetary Laboratory, University of Arizona, Tucson, AZ 85721, USA
[5] IAPS—INAF Istituto di Astrofisica e Planetologia Spaziali, 00133 Roma, Italy
[6] Laboratoire de Physique des Plasmas, CNRS, 91128 Palaiseau, France
Received 2024 June 7; revised 2024 July 1; accepted 2024 July 8; published 2024 July 25

Abstract

Plasma turbulence involves complex, nonlinear interactions of electromagnetic fields and charged particles across multiple scales. Studying these phenomena in space plasmas, like the solar wind, is facilitated by the intrinsic scale separations and the availability of in situ spacecraft observations. However, the single-point or single-scale configurations of current spacecraft limit our understanding of many properties of the turbulent solar wind. To overcome these limitations, multipoint measurements spanning a range of characteristic scales are essential. This Letter prepares for the enhanced measurement capabilities of upcoming multispacecraft missions by demonstrating that higher-order statistics, specifically kurtosis, as a baseline for intermittency can be accurately measured. Using synthetic turbulent fields with adjustable intermittency levels, we achieve scale separations analogous to those in the solar wind and apply these techniques to the planned trajectories of the HelioSwarm mission. This approach promises significant advancements in our understanding of plasma turbulence.

Unified Astronomy Thesaurus concepts: Solar wind (1534); Interplanetary turbulence (830); Theoretical techniques (2093)

1. Introduction

Initial observations of atmospheric turbulence by Richardson (1922) suggested the existence of space-filling eddies of all sizes. This inspired the widely invoked Kolmogorov theory (Kolmogorov 1941, hereafter K41). This theoretical development assumed, as one of the fundamental hypotheses of similarity, that the viscosity and the average energy dissipation rate uniquely determine the statistical properties of the turbulent field. However, early results from fluid experiments showed intermittent behavior within the dissipation range evidenced by a nonuniform distribution of energy at small scales (Batchelor & Townsend 1949). These observations led to modifications in the theory of turbulence to include the patchy bursts of dissipation in the form of a locally averaged energy dissipation rate rather than a globally averaged one. This is the so-called refined similarity hypothesis (Oboukhov 1962; Kolmogorov 1962). After the observation of dissipation-range intermittency, it was also observed in the inertial range with the experimental work of Anselmet et al. (1984) and later confirmed by Gagne (1987).

The phenomenology of intermittency, associated with an uneven distribution of energy in space, describes a turbulent medium with a relatively small number of strong, nonspace-filling discontinuities, as opposed to the original Richardson description of a large number of uniformly distributed discontinuities (Frisch 1995). This paradigmatic change inspired several theoretical works that aimed at an accurate phenomenological description of higher-order moments that depart from the K41 prescription (Mandelbrot 1974; Frisch et al. 1978; Benzi et al. 1984; Meneveau & Sreenivasan 1987; She & Leveque 1994). It should be emphasized that these descriptions of intermittency are physically plausible and consistent with observations, but the refined similarity hypothesis itself remains a useful conjecture (Wang et al. 1996; Chen et al. 1997) though still unproven to our knowledge.

Intermittency in the solar wind was first observed by Burlaga (1991a, 1991b, 1991c, 1992). Subsequent observations confirmed the earlier findings of intermittent features of the solar wind evidenced by departures of high-order moments from the linear scaling of K41 or, equivalently, as a (more or less pronounced) departure from Gaussianity (Marsch & Tu 1997; Sorriso-Valvo et al. 1999; Padhye et al. 2001; Vörös et al. 2002; Koga et al. 2007; Wan et al. 2011; Chasapis et al. 2020; Chhiber et al. 2020; Roberts et al. 2022). Extensions of the hydrodynamic intermittency correction to magnetohydrodynamics (MHD) were developed (Carbone 1993) together with the possibility of distinguishing between fluid and magneto-fluid turbulence (Carbone et al. 1995).

In MHD and in the solar wind, as in hydrodynamics, the essential physics of intermittency is the observed nonuniformity of the energy density (Marsch et al. 1996). However, again one should note that the theoretical basis for intermittency in MHD remains unproven, as it is in hydrodynamics. Moreover, the precise form of refined similarity in MHD is not well established—see, e.g., Merrifield et al. (2005)—and remains based on phenomenological arguments (e.g., Chandran et al. (2015).).

In MHD, the manifestation of intermittency has been directly associated with the bursts of kinetic energy and dissipation generated at reconnection sites and, more generally, with current sheets and discontinuities (Matthaeus & Lamkin 1986; Carbone et al. 1990; Servidio et al. 2010; Wan et al. 2012;

Matthaeus et al. 2015). Novel methods for the detection of intermittent structures were developed based on wavelet analysis (Farge 1992; Veltri & Mangeney 1999; Bruno et al. 2001) or the partial variance of increments (PVI; Greco et al. 2008, 2018).

The subsequent applications of these methods originated a vast section of literature that relates intermittent events with kinetic effects such as particle diffusion and heating (Osman et al. 2012a, 2012b; Tessein et al. 2013; Chasapis et al. 2015; Tessein et al. 2015; Mallet et al. 2019; González et al. 2024), as well as in the macroscopic description of the solar wind as composed of adjacent flux tubes with sharp (discontinuous) boundaries (Borovsky 2008; Kittinaradorn et al. 2009; Tessein et al. 2016; Pecora et al. 2019, 2021).

More recent investigations using the Magnetospheric Multiscale (MMS) mission (Burch et al. 2016) and Cluster (Escoubet et al. 2001) have explored similar topics (Chhiber et al. 2018; Roberts et al. 2022). However, even though the MMS mission provides multipoint measurements, the separations between spacecraft do not allow for multiscale analyses. The methods explored in the present Letter extend the methods developed for MMS (Chhiber et al. 2018). Upcoming missions like HelioSwarm (HS; Spence 2019; Klein et al. 2023) and Plasma Observatory (Retinò et al. 2022; Marcucci & Retinò 2024) aim to rectify these limitations by providing simultaneous measurements over a range of scales.

Simulations, both of MHD and kinetic plasma, have been very useful in elucidating statistical properties of intermittency (Biskamp & Müller 2000; Leonardis et al. 2016; Wan et al. 2016). Parashar et al. (2015) showed that the intermittency level increases with the Reynolds number, highlighting the relevance of system size in such investigations. Results complementary to the present work have been presented recently, quantifying intermittency and employing PVI statistics and magnetic field increments using HS-like trajectories (Guerrero Guio et al. 2024).

The Letter is organized as follows. We first provide a brief description of HS configuration parameters in Section 2 that will be used in the next sections. The model used to obtain a turbulent and intermittent magnetic field with scaling properties and ranges of scales similar to the solar wind is described in Section 3. The results are presented in Section 4. Finally, in the last section, conclusions are drawn together with a discussion of the implications of these findings for future multispacecraft missions.

2. HS Configuration

Since at least the 1980 Plasma Turbulence Explorer Study Group Report (Montgomery et al. 1980), the necessity of a multispacecraft observatory for measuring the multiscale characteristics of plasma turbulence has been recognized. Over the past several decades, various concepts for such missions have been proposed, including the CrossScale mission (Schwartz et al. 2009).

The forthcoming HS mission (Spence 2019; Klein et al. 2023) features an observatory of nine spacecraft that will provide in situ measurements of near-Earth plasmas, encompassing the magnetosphere and the solar wind. It will provide simultaneous measurements, with interspacecraft separations ranging from fluid to ion-kinetic scales. These measurements span a three-dimensional volume to provide adequate coverage of fundamental turbulence statistics (Section 4.5.1,

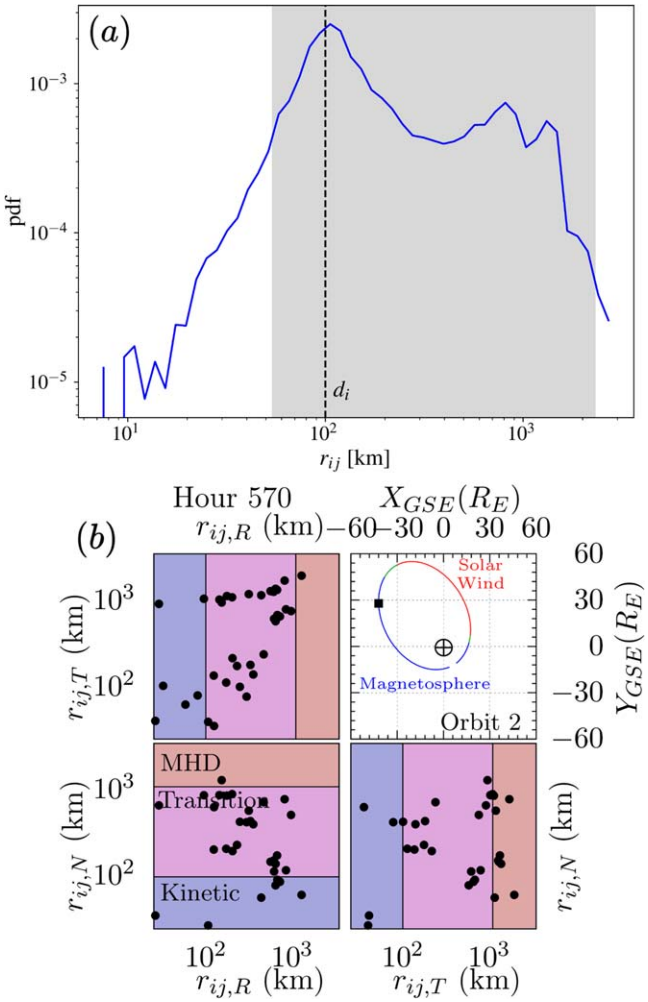

Figure 1. (a) Probability density function of HS interspacecraft separations throughout the entire duration of the mission. A nominal d_i scale of 100 km is indicated with a vertical dashed line. The configuration used in this work spans the range of scales indicated by the gray-shaded area. ((b), upper right) The black square represents the positions of HS at hour 570 of the planned trajectories (in Earth radii; geocentric solar ecliptic coordinate system). The orbit is color coded by nominal positions of the magnetosphere (blue), pristine solar wind (red), and magnetically connected regions (green). The other three panels illustrate the 36 separations between the nine spacecraft, projected onto an RTN reference frame. The three stripes in each panel indicate the MHD, transition, and kinetic ranges.

Klein et al. 2023). For direct comparison of orbital parameters with those of the solar wind, we use nominal values at 1 au for the ion skin depth $d_i = 100$ km (Verscharen et al. 2019) and the correlation length $\lambda_c = 10^6$ km (Matthaeus et al. 1999). These two scales are generally indicative of the extension of the so-called turbulent inertial range.

The distribution of the range of scales spanned by spacecraft separations, using HS Design Reference Mission trajectories, is shown in Figure 1(a). The interspacecraft separations are measured as $r_{ij} = |\boldsymbol{r}_i - \boldsymbol{r}_j|$, where i, j is any pair of spacecraft i, $j = 1,...9$, and $j > i$. The spacecraft observatory will cover about 2 orders of magnitude of scale separations across the lower end of the inertial range (marked by d_i). For the present work, we have selected hour 570 of the above-mentioned designed trajectories as an example of the observatory having good three-dimensional baseline separations spanning MHD, transition, and ion-kinetic scales. At that time, the spacecraft are separated by 54 to 2327 km, as indicated by the shaded area in

Figure 1(a). The position of HS and the vector components of the $C_9^2 = 36$ baselines, projected onto a radial–tangential–normal (RTN) coordinate system, is illustrated in Figure 1(b). As the orbit remains nearly inertially fixed, the apogee undergoes rotation over the course of 1 year, enabling the observatory to sample the pristine solar wind, the magnetosphere, and areas magnetically connected between these two. The HS configuration at hour 570 was selected since it spans over 1 order of magnitude in scales, making it ideal for examining scale-dependent quantities, such as kurtosis. Moreover, a similar configuration is attained across all three spatial regions (i.e., pristine solar wind, foreshock, and magnetosphere), providing the possibility to perform similar analyses in different environments. For all subsequent analyses, the configuration of the spacecraft remains constant. The virtual spacecraft travel along parallel trajectories, with the fields generated as if they were time series along these paths.

3. Synthetic Turbulence Model

The model employed for this work reproduces a synthetic three-dimensional turbulent solenoidal field with non-Gaussian (intermittent) properties based on the p-model of Meneveau & Sreenivasan (1987), as first described in Malara et al. (2016). The model does not generate coherent structures but rather statistics of the fluctuations in accordance with that of an intermittent field. Such a field can be directly identified with a magnetic field. The model constructs the magnetic field by superimposing wavelets at various scales from the box size to a desired resolution. The advantage offered by this approach is that at any position, the magnetic field is calculated as the sum of contributions from the wavelets encompassing the point in question. This drastically reduces the number of operations needed to compute the field compared to Fourier methods. The computational time required to evaluate the fields increases linearly with the number n of scales at which the wavelets are defined. The spatial resolution is proportional to 2^{-n}. This scaling property enables the generation of fields with large spectral bandwidth at low computational costs. Since the wavelets are analytically defined, the field is also analytically defined. Consequently, the field value at any position is computed in real time without the need for a fixed grid. This eliminates the necessity of storing the field in memory, making the algorithm highly suitable for the objectives of this study where we consider a realistic extension of the inertial range. These synthetic turbulent and intermittent magnetic fields have been used for the study of energetic particle diffusion and modeling solar wind fast-speed streams (Pucci et al. 2016; Perri et al. 2017, 2019; Valentini et al. 2019).

The field is constructed iteratively by partitioning the flux of spectral energy $\mathcal{E}_{l_m}$ within a volume of scale l_m following the prescription of the p-model. In this process, half of the subvolume at scale l_{m+1} receives the fraction $\mathcal{E}_{l_{m+1}} = 2p\mathcal{E}_{l_m}$, while the other half receives $\mathcal{E}_{l_{m+1}} = 2(1-p)\mathcal{E}_{l_m}$. When $p = 1/2$, the two subvolumes at scale l_{m+1} receive equal energy. For $p \neq 1/2$, intermittency arises due to the imbalance in energy partitioning. This procedure is carried out from the largest (box) scale to a desired minimum resolution. In principle, the domain is periodic, but the periodicity length can be set to be arbitrarily large with respect to the correlation length.

For our purposes, we set the periodicity length (corresponding to the side of the fictitious box in which the fields are defined) to be 80 correlation lengths (80×10^6 km). As stated earlier, the fields are not defined on a numerical grid, but instead, they can be evaluated at any desired point through an analytical definition. In order to avoid periodicity effects, we restrain our analyses in a subdomain of side $40\lambda_c$. We will consider both an isotropic and an anisotropic system.

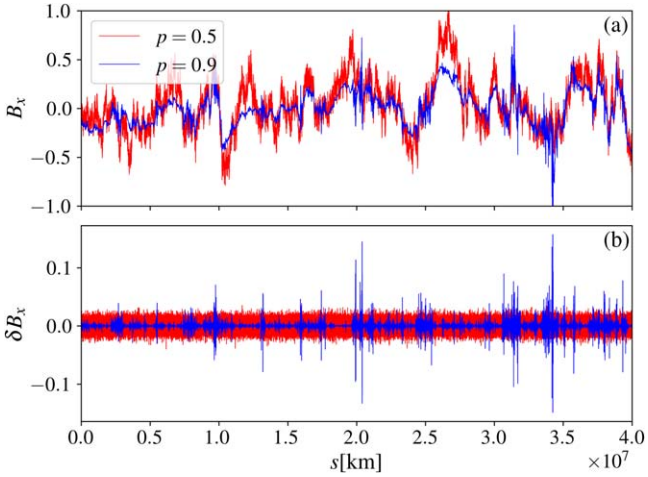

Figure 2. (a) One magnetic field component, B_x, for intermittency levels $p = 0.5$ (red) and $p = 0.9$ (blue) sampled along a line s in any direction (the system is isotropic) with resolution $\delta s \simeq 30$ km. (b) Increments $\delta B_x = B_x(s) - B_x(s + \delta s)$. The field with no intermittency, $p = 0.5$, does not show any "bursty" features. The field with higher intermittency ($p = 0.9$) shows large localized spikes, an indicator of intermittency.

For the former, the smallest scale is set to correspond to the ion inertial length in the solar wind at 1 au ($d_i = 100$ km; Verscharen et al. 2019). The spacecraft "time series" have a sampling resolution of 30 km (or, equivalently, a 75 ms with a nominal solar wind speed of 400 km s^{-1}). We generated three sets of magnetic fields with increasing levels of intermittency. The field with $p = 0.5$ has Gaussian increments (no intermittency). The other two fields with $p = 0.7$ and $p = 0.9$ show increasing levels of intermittent behavior, as seen in Figure 2 for the two extreme cases of $p = 0.5$ and $p = 0.9$. In that figure, we show the magnetic field component B_x obtained on a line sampling $40\lambda_c$ along a generic direction s. For the anisotropic case, we focus on the intermittency level $p = 0.7$, and for reasons detailed below, the smallest scale is set to 0.015 km and the resolution of the time series is 60 km (or 150 ms).

The three sets of fields for the isotropic case have been generated imposing a nominal spectral slope of $-5/3$ within the inertial range, as is frequently observed in the solar wind (Kiyani et al. 2015). Below the chosen smallest scale (d_i), the spectrum decays exponentially. The field with $p = 0.9$ shows a slightly steeper slope as higher levels of intermittency are expected to modify the slope of the power spectrum (Oboukhov 1962; Kolmogorov 1962.) Figure 3(a) shows the power spectra for the three fields (with the different intermittency levels); indicated are the scales corresponding to λ_c and d_i and the range of scales covered by HS for the selected Design Reference Mission hour as a shaded area.

To investigate possible effects due to anisotropy, a case relevant to the solar wind, we obtain a realization of fields with different spectral slopes in the directions parallel and perpendicular to the mean magnetic field with a fixed $p = 0.7$. The anisotropy is obtained by elongating the support of the wavelets in the direction parallel to the mean magnetic field, as explained in Malara et al. (2016). As a result of that

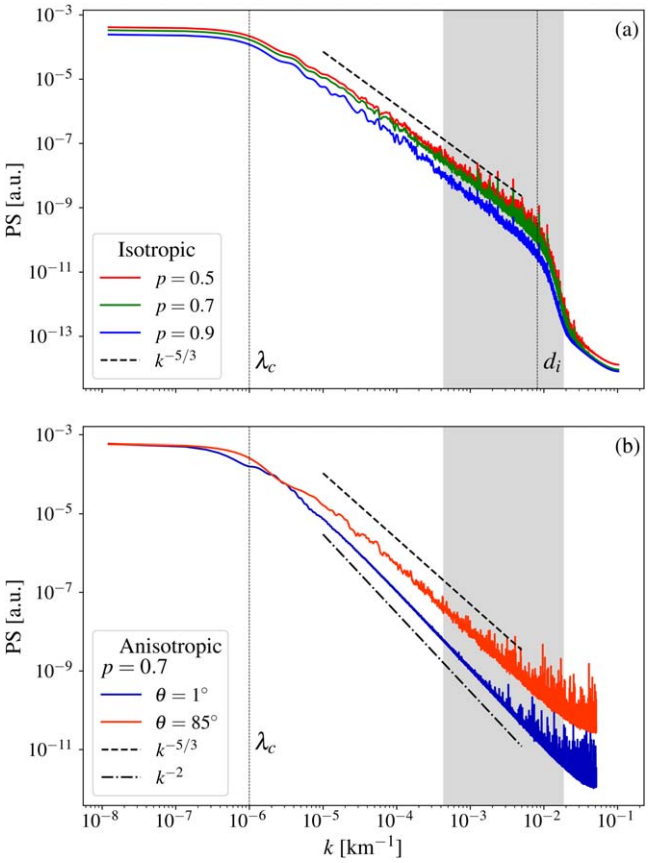

Figure 3. Magnetic field power spectra computed over single spacecraft trajectories and then averaged for (a) isotropic and (b) anisotropic cases. $k^{-5/3}$ and k^{-2} dashed and dotted–dashed lines are added as reference. The gray-shaded area indicates the range of scales covered by the HS separations. In (a) it is evident that higher intermittency ($p = 0.9$) generates slightly steeper spectra, though the extension of the inertial range remains intact. Correlation and "dissipation" scales are indicated with vertical dotted lines. In (b) the spectra are computed when the HS formation flies at angles $\theta = 1°$ and $\theta = 85°$ with respect to the mean field direction. The apparent flattening is only due to a downsampling of the measurements. The spectra would have a decay similar to that occurring near d_i in (a) at $k \sim 67$. The slopes have also been estimated using a fit in the region indicated by the reference lines obtaining -1.91 and -1.64 for $\theta = 1°$ and $\theta = 85°$ respectively.

procedure, the parallel spectrum decays exponentially at scales larger than that in the perpendicular direction. To ensure that the spectrum in the parallel direction does not fall off exponentially in the range of scales covered by HS, we shifted the onset of the exponential decay to these smaller scales.

In this realization, we fly the HS observatory at eight different angles θ ranging from 1° to 85° with respect to a mean field $B_0\hat{z}$. In Figure 3(b) we show the magnetic field power spectra, and as in (a), the correlation length is indicated with a vertical line, and the scales spanned by the observatory are represented by the gray-shaded area. In this case, the spectra do not show the exponential falloff as they extend to k's larger than those shown in Figure 3(a). The smallest scale in this case is 0.015 km, which corresponds to $k \sim 67$. The apparent flattening of the spectra at large k's is due to downsampling of the fields to obtain reasonable sizes of the data arrays.

4. Results

Formally, intermittency is the deviation of the distribution of some quantity from a Gaussian distribution. This deviation is

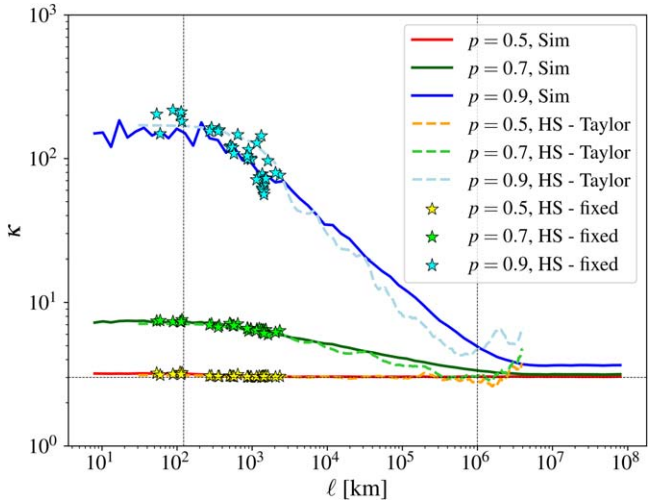

Figure 4. Kurtosis of the longitudinal magnetic field increments. Solid lines are obtained from millions of random paired points scattered throughout the whole volume—see case (i). Dashed lines result from a Taylor-like approach on single-spacecraft trajectories and are then averaged; see case (ii). Symbols are obtained from fixed interspacecraft separations; see case (iii).

expressed by extreme values that are more probable than those observed in a normally distributed population. One way to quantify this is to compare the fourth-order to the second-order moment squared of the scalar increments δf, defined as the difference $f(\boldsymbol{x}) - f(\boldsymbol{x} + \boldsymbol{\ell})$ between two points in space separated by a (vector) lag $\boldsymbol{\ell}$. We use the longitudinal increments of the magnetic field $\delta b_\ell = \delta \boldsymbol{b} \cdot \hat{\ell} = (\boldsymbol{B}_i(\boldsymbol{x}_i) - \boldsymbol{B}_j(\boldsymbol{x}_j)) \cdot \hat{\ell}$ where $\boldsymbol{B}_i(\boldsymbol{x}_i)$ is the magnetic field measured at position $\boldsymbol{x}_i$, $\boldsymbol{B}_j$ is at position $\boldsymbol{x}_j = \boldsymbol{x}_i + \boldsymbol{\ell}$, and $\hat{\ell}$ is the unit vector along the $\boldsymbol{\ell}$ direction. We operationally define the scale-dependent kurtosis as

$$\kappa(\ell) = \frac{\langle \delta b_\ell^4 \rangle}{\langle \delta b_\ell^2 \rangle^2}, \tag{1}$$

where $\langle . \rangle$ indicates an ensemble average (Frisch 1995). When the increments of a scalar field follow a Gaussian distribution, $\kappa(\ell) = \kappa = 3$. The presence of extreme fluctuations produces values of κ larger than 3. We measure the scale-dependent kurtosis κ by adapting the definition in Equation (1) to four different scenarios.

(i) We first need the accurate kurtosis obtainable from the entire sample of the synthetic fields. These are the data to which the spacecraft sample results are going to be compared. Since the fields are not defined on a grid, we choose several million pairs of points (over which the ensemble average of Equation (1) is calculated) at random positions within the domain. Separations are randomly oriented with magnitudes equally spaced, ranging from the domain size (8×10^7 km) to 8 km. This approach provides the solid lines in Figure 4 that are representative of the kurtosis of the synthetic fields over the whole domain.

For the next three approaches, we use the HS trajectories.

(ii) To evaluate the scale-dependent kurtosis, we use spatial increments along the trajectory of each spacecraft. These increments are represented by $\delta \boldsymbol{b}_\ell = (\boldsymbol{B}_i(\boldsymbol{x}_i) - \boldsymbol{B}_i(\boldsymbol{x}_i + \ell_i))$, where ℓ_i denotes the spatial increments along the trajectory of spacecraft i. This method is similar to measuring temporal increments in a spacecraft's time series and then applying the Taylor hypothesis exactly, which assumes that the structures

observed in the flow are "frozen" and advected past the spacecraft without changing shape (Taylor 1938). The ensemble average is taken along each trajectory, and then we average the resulting κ over the nine trajectories for additional statistical weight. Good agreement of the HS–Taylor-like scale-dependent kurtosis with the validated one of approach (i) is attained within the range of scale up to $1/10$ of the correlation length.

(iii) This approach fully exploits HS's multipoint potential. The scale-dependent nature of kurtosis is analyzed without the need for Taylor's hypothesis, thus avoiding problems of spacetime correlation, especially at smaller scales. Instead, the increments are computed at the fixed separations between the spacecraft, $\delta\boldsymbol{b}(\ell_{ij}) = (\boldsymbol{B}_i(\boldsymbol{x}_i) - \boldsymbol{B}_j(\boldsymbol{x}_j))$, where $\boldsymbol{B}_i(\boldsymbol{x}_i)$ is the magnetic field at the position $\boldsymbol{x}_i$ of the ith spacecraft, $\ell_{ij} = \boldsymbol{x}_j - \boldsymbol{x}_i$, and the ensemble average is taken over the whole trajectory. The simultaneous observations from nine seperate spacecraft allow for 36 values of kurtosis to be computed with different lags; these are shown by the symbols in Figure 4.

(iv) Finally, we analyzed the effects of increments measured between different spacecraft, as discussed in previous studies (Horbury 2000; Osman et al. 2011). Similar to strategy (ii), we assume the validity of the Taylor hypothesis. Using this "modified" Taylor hypothesis, the magnetic field increments measured across different spacecraft time series are defined as $\delta\boldsymbol{b}(\ell_{ij}) = (\boldsymbol{B}_i(\boldsymbol{x}_i) - \boldsymbol{B}_j(\boldsymbol{x}_j + \ell_j))$, where ℓ_j represents the spatial increments along the trajectory of spacecraft j. Contrary to case (iii), this approach results in 36 lines instead of 36 points. The outcomes from this method are nearly identical to those obtained in the previous cases and are therefore not displayed below.

All methods show high levels of agreement, regardless of the intermittency levels. As expected, the field with Gaussian increments ($p = 0.5$) shows a constant value of $\kappa = 3$ across all scales. Of particular relevance is the accuracy of the scale-dependent kurtosis obtained by the spacecraft using their fixed separations without the employment of the Taylor hypothesis. The results shown in Figure 4 are obtained using the isotropic fields. In the following, we investigate the effects of anisotropy on the evaluation of scale-dependent kurtosis.

For the analysis of the scale-dependent kurtosis in an anisotropic medium, we use approaches (i) and (iii) described above. Approach (i) is used to show agreement of the results with the global statistical properties of the fields, and (iii) exploits the unprecedented capabilities of novel multiscale missions. In the latter case, two different angles need to be defined, as will be relevant below. θ is the angle of the (parallel) trajectories with respect to $\hat{z}$. φ is the angle between the vector separations $\boldsymbol{r}_{ij}$ with $\hat{z}$.

The "reference" scale-dependent kurtosis obtained using method (i) for angles ranging from $\theta = 1^\circ$ to $\theta = 85^\circ$ is illustrated in Figure 4(a). Higher levels of intermittency are observed for directions parallel to the mean field. This can be understood in the context of the present model as follows. The anisotropy arises from "splitting" the energy content of a subvolume into subdomains elongated in a preferred direction, as described by Malara et al. (2016). This elongation of subdomains implies that the same value of kurtosis seen in the perpendicular direction is achieved in the parallel direction at much larger scales. Furthermore, it is possibly reasonable to expect higher kurtosis in this direction, considering the heuristic

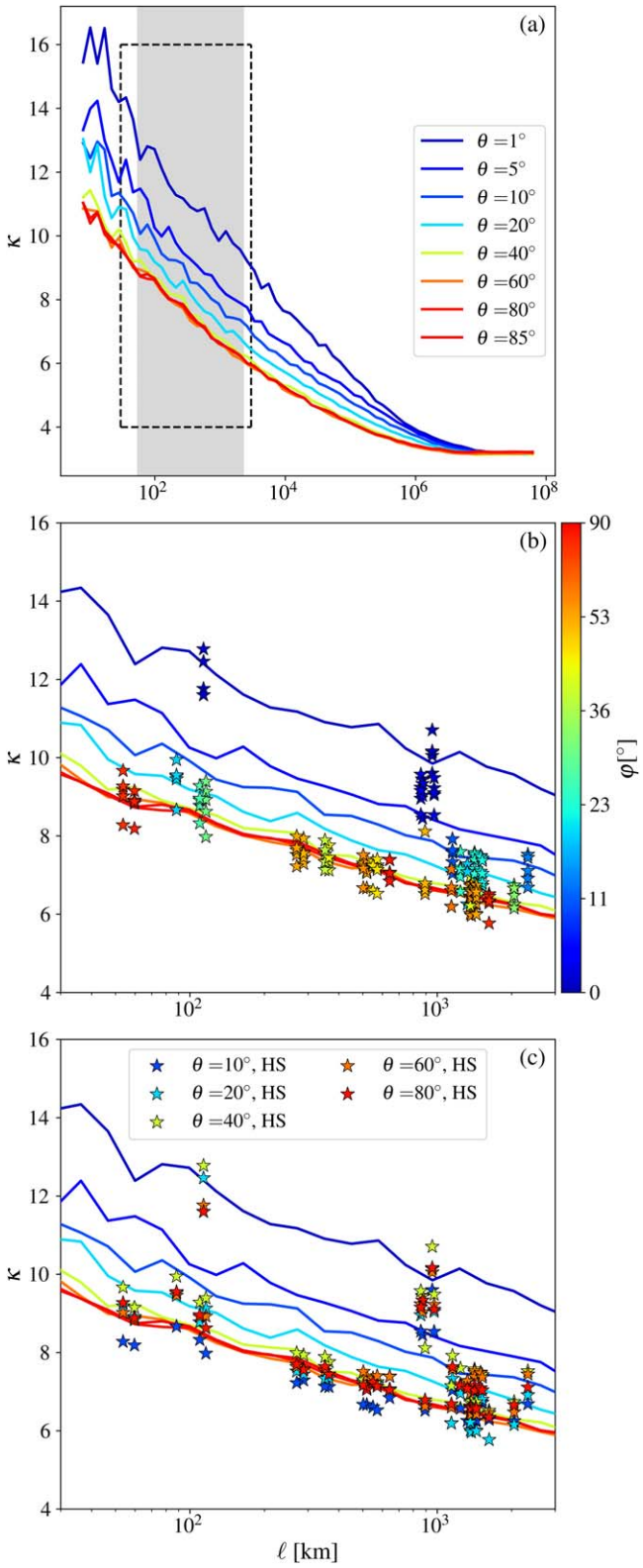

Figure 5. (a) Kurtosis obtained from the anisotropic fields in different directions θ with respect to the mean field using method (i). Indicated is the range of scales spanned by the spacecraft as a gray-shaded area. The dashed box indicates the region focus of (b) and (c). In (b) the HS κ values (symbols; method (iii)) are colored by the angle φ the vector separation $\boldsymbol{r}_{ij}$ makes with the $\hat{z}$ direction. In (c), the stars are colored by the angle θ at which the observatory flies with respect to $\hat{z}$. Notice the good agreement of method (iii) with the expected values when the angle φ is considered.

interpretation of kurtosis as a measure of the inverse of the filling factor of the intermittent features (Frisch 1995).

We then explored the accuracy of determining the scale-dependent kurtosis using the HS pairs, as outlined in strategy (iii). In this case, along with considering the angle θ formed by the trajectory with the mean field direction $\hat{z}$, we also need to account for the angle φ formed by the vector separation $\boldsymbol{r}_{ij}$ with respect to $\hat{z}$. As depicted in Figure 4(b), where the symbols are color coded by the angle φ that each HS pair forms with $\hat{z}$, it becomes apparent that the spacecraft ability to capture different kurtosis values hinges not only on their relative distances but also on their orientation. Conversely, neglecting the pair's orientation with respect to the mean field, as in (c) where the symbols are color coded with the angle θ formed by the trajectory with $\hat{z}$, leads to less precise kurtosis measurements. Although the general scale-dependent trend remains discernible, certain values deviate due to the pairs sampling diverse orientations relative to the mean field.

To maintain clarity, fewer θ trajectories are displayed in Figures 5(b) and (c) as their overall behavior remains consistent. Only the trajectory at $\theta = 1°$ tends to slightly overestimate kurtosis values. This can be rationalized by considering that an almost perfectly parallel trajectory, when no dynamical activity is present, would register smaller variations along its path. Consequently, the spacecraft essentially measure similar kurtosis values along their trajectory as those observed at their initial position, making it unrepresentative of the entire domain.

5. Conclusions

In the new era of multipoint multiscale space missions, it is imperative to enhance our management of the increasing volume and complexity of data. In this study, we presented an analysis of the remarkable potential of the forthcoming HS mission in measuring scale-dependent kurtosis. We demonstrated that the HS observatory not only provides adequate coverage for accurate convergence of this higher-order statistic but also allows for a comprehensive investigation of its nature in an anisotropic medium such as the solar wind.

We employed a model for generating synthetic turbulence fields that does not rely on a fixed grid, enabling the investigation of a range of spatial scales similar to those of the solar wind. The analyses were performed in a three-dimensional domain of size $80 \times \lambda_c = 8 \times 10^7$ km per side, with characteristic "dissipation" scales (the scale at which the power spectra have an exponential decay) $d_i = 100$ km and 0.015 km for the isotropic and anisotropic systems, respectively.

We selected a time in the current Design Reference Mission trajectories of HS when the spacecraft had separations ranging from 54 to 2327 km. This specific configuration, which spans more than 1 order of magnitude in scales, is optimal for analyzing scale-dependent quantities such as kurtosis.

Initially, we assessed the accuracy of kurtosis estimates by HS pairs in an isotropic medium. We compared the scale-dependent kurtosis obtained using four different strategies. (i) We used millions of pairs with random orientations and increasing separations to measure scale-dependent kurtosis homogeneously throughout the entire domain from 8 to 8×10^8 km. This measure serves as a reference for the other methods. (ii) We employed magnetic field measurements along single-spacecraft trajectories and applied the Taylor hypothesis to compute the kurtosis. For the isotropic case, this measure (averaged over all nine trajectories) provided an accurate prediction for scales up to $1/10$ of the correlation length, with deviations likely due to the lower statistical weight of the largest lags. (iii) We used fixed separations between spacecraft pairs to evaluate kurtosis, and the HS observatory allowed for up to 36 independent estimates, reported to be accurate regardless of the intermittency level. (iv) We applied a modified Taylor hypothesis, computing increments across different spacecraft pairs. This method also agreed with the others (not shown), demonstrating the robustness of the analyses applicable to the anisotropic case.

Next, we introduced spectral anisotropy of the fields, enforcing a steeper power spectrum for the magnetic field in a specified direction (e.g., $\hat{z}$). We obtained a magnetic field with a spectrum following a $k^{-5/3}$ power law in the perpendicular plane (relative to $\hat{z}$) and k^{-2} in the parallel direction. We compared the results from methods (i) and (iii). From (i), we observed that scale-dependent kurtosis had higher values when sampled in the parallel direction, reflecting the model-generated anisotropy. Using method (iii), there are at least two possible ways to analyze the results in the anisotropic medium. If results are cast in a fashion similar to the isotropic case, one perceives that the overall scale-dependent trend is somewhat maintained even though nonnegligible variations are present (Figure 5(c)). The nature of these variations is unveiled when the values are associated with the angle formed by the spacecraft pair with the preferred direction (Figure 5(b)). In this case, an order is recovered, and it shows that the "correct" value of kurtosis is obtained when the orientation of the pair is taken into consideration more so than with respect to the orientation of the trajectory itself.

The results obtained in this work using a synthetic model for a turbulent magnetic field with scale separations nominally identical to those of the solar wind further support the effectiveness of multipoint multiscale missions for the observation of quantities as not previously possible in space plasmas. The general accordance and robustness of the results preannounce reliable scale-dependent measures in the solar wind. This work contributes to the growing body of research dedicated to fully exploiting future multispacecraft data (Maruca et al. 2021; Pecora et al. 2023; Broeren et al. 2024) in preparation for missions such as HS (Spence 2019; Klein et al. 2023) and Plasma Observatory (Retinò et al. 2022; Marcucci & Retinò 2024).

Acknowledgments

This work is supported by NASA MMS Mission under grant No. 80NSSC19K0565 at the University of Delaware and by the HelioSwarm Mission. F.P. acknowledges the project "Data-based predictions of solar energetic particle arrival to the Earth: ensuring space data and technology integrity from hazardous solar activity events" (CUP H53D23011020001) financed by the European Union—Next Generation EU PIANO NAZIONALE DI RIPRESA E RESILIENZA (PNRR) Missione 4 "Istruzione e Ricerca" - Componente C2 Investimento 1.1, "Fondo per il Programma Nazionale di Ricerca e Progetti di Rilevante Interesse Nazionale (PRIN)" Settore PE09. We acknowledge EuroHPC JU for awarding project access to MeluXina CPU at LuxProvide (LU).

ORCID iDs

Francesco Pecora https://orcid.org/0000-0003-4168-590X
Francesco Pucci https://orcid.org/0000-0002-5272-5404
Francesco Malara https://orcid.org/0000-0002-5554-8765
Kristopher G. Klein https://orcid.org/0000-0001-6038-1923
Maria Federica Marcucci https://orcid.org/0000-0002-5002-6060
Alessandro Retinò https://orcid.org/0000-0001-5824-2852
William Matthaeus https://orcid.org/0000-0001-7224-6024

References

Anselmet, F., Gagne, Y., Hopfinger, E. J., & Antonia, R. A. 1984, JFM, 140, 63
Batchelor, G. K., & Townsend, A. A. 1949, RSPSA, 199, 238
Benzi, R., Paladin, G., Parisi, G., & Vulpiani, A. 1984, JPhA, 17, 3521
Biskamp, D., & Müller, W.-C. 2000, PhPl, 7, 4889
Borovsky, J. E. 2008, JGRA, 113, A08110
Broeren, T., Klein, K. G., & TenBarge, J. M. 2024, E&SS, 11, e2023EA003369
Bruno, R., Carbone, V., Veltri, P., Pietropaolo, E., & Bavassano, B. 2001, P&SS, 49, 1201
Burch, J. L., Moore, T. E., Torbert, R. B., & Giles, B. L. 2016, SSRv, 199, 5
Burlaga, L. F. 1991a, JGRA, 96, 5847
Burlaga, L. F. 1991b, GeoRL, 18, 69
Burlaga, L. F. 1991c, GeoRL, 18, 1651
Burlaga, L. F. 1992, JGRA, 97, 4283
Carbone, V. 1993, PhRvL, 71, 1546
Carbone, V., Veltri, P., & Bruno, R. 1995, PhRvL, 75, 3110
Carbone, V., Veltri, P., & Mangeney, A. 1990, PhFl, 2, 1487
Chandran, B. D. G., Schekochihin, A. A., & Mallet, A. 2015, ApJ, 807, 39
Chasapis, A., Matthaeus, W. H., Bandyopadhyay, R., et al. 2020, ApJ, 903, 127
Chasapis, A., Retinò, A., Sahraoui, F., et al. 2015, ApJL, 804, L1
Chen, S., Sreenivasan, K. R., Nelkin, M., & Cao, N. 1997, PhRvL, 79, 2253
Chhiber, R., Chasapis, A., Bandyopadhyay, R., et al. 2018, JGRA, 123, 9941
Chhiber, R., Goldstein, M. L., Maruca, B. A., et al. 2020, ApJS, 246, 31
Escoubet, C. P., Fehringer, M., & Goldstein, M. 2001, AnGeo, 19, 1197
Farge, M. 1992, AnRFM, 24, 395
Frisch, U. 1995, Turbulence: the legacy of AN Kolmogorov (Cambridge: Cambridge Univ. Press)
Frisch, U., Sulem, P.-L., & Nelkin, M. 1978, JFM, 87, 719
Gagne, Y. 1987, PhD thesis, Université Joseph Fourier (Grenoble; 1971-2015)
González, C. A., Verniero, J. L., Bandyopadhyay, R., & Tenerani, A. 2024, ApJ, 963, 148
Greco, A., Chuychai, P., Matthaeus, W. H., Servidio, S., & Dmitruk, P. 2008, GeoRL, 35, L19111
Greco, A., Matthaeus, W. H., Perri, S., et al. 2018, SSRv, 214, 1
Guerrero Guio, A. F., Agudelo Rueda, J. A., & Vargas Domínguez, S. 2024, FrASS, 11, 1323993
Horbury, T. S. 2000, in ESA Special Publication, Cluster-II Workshop Multiscale / Multipoint Plasma Measurements, 449, ed. R. A. Harris (Paris: European Space Agency), 89
Kittinaradorn, R., Ruffolo, D., & Matthaeus, W. H. 2009, ApJL, 702, L138
Kiyani, K. H., Osman, K. T., & Chapman, S. C. 2015, RSPTA, 373, 20140155
Klein, K. G., Spence, H., Alexandrova, O., et al. 2023, SSRv, 219, 74
Koga, D., Chian, A. C.-L., Miranda, R. A., & Rempel, E. L. 2007, PhRvE, 75, 046401
Kolmogorov, A. 1941, DoSSR, 30, 301
Kolmogorov, A. N. 1962, JFM, 13, 82
Leonardis, E., Sorriso-Valvo, L., Valentini, F., et al. 2016, PhPl, 23, 022307
Malara, F., Di Mare, F., Nigro, G., & Sorriso-Valvo, L. 2016, PhRvE, 94, 053109
Mallet, A., Klein, K. G., Chandran, B. D. G., et al. 2019, JPlPh, 85, 175850302
Mandelbrot, B. B. 1974, JFM, 62, 331
Marcucci, M. F., Retinò, A. & the Plasma Observatory team 2024, in EGU General Assembly Conf. Abstracts, 11903
Marsch, E., & Tu, C.-Y. 1997, NPGeo, 4, 101
Marsch, E., Tu, C. Y., & Rosenbauer, H. 1996, AnGeo, 14, 259
Maruca, B. A., Agudelo Rueda, J. A., Bandyopadhyay, R., et al. 2021, FrASS, 8, 108
Matthaeus, W. H., & Lamkin, S. L. 1986, PhFl, 29, 2513
Matthaeus, W. H., Smith, C. W., & Bieber, J. W. 1999, AIP Conf. Proc., 471 (Melville, NY: AIP), 511
Matthaeus, W. H., Wan, M., Servidio, S., et al. 2015, RSPTA, 373, 20140154
Meneveau, C., & Sreenivasan, K. R. 1987, PhRvL, 59, 1424
Merrifield, J. A., Müller, W.-C., Chapman, S. C., & Dendy, R. O. 2005, PhPl, 12, 022301
Montgomery, D., et al. 1980, Report of the NASA Plasma Turbulence Explorer Study Group 715-78, NASA, Jet Propulsion Laboratory, Pasadena, CA
Oboukhov, A. M. 1962, JFM, 13, 77
Osman, K. T., Matthaeus, W. H., Hnat, B., & Chapman, S. C. 2012a, PhRvL, 108, 261103
Osman, K. T., Matthaeus, W. H., Wan, M., & Rappazzo, A. F. 2012b, PhRvL, 108, 261102
Osman, K. T., Wan, M., Matthaeus, W. H., Weygand, J. M., & Dasso, S. 2011, PhRvL, 107, 165001
Padhye, N. S., Smith, C. W., & Matthaeus, W. H. 2001, JGRA, 106, 18635
Parashar, T. N., Matthaeus, W. H., Shay, M. A., & Wan, M. 2015, ApJ, 811, 112
Pecora, F., Greco, A., Hu, Q., et al. 2019, ApJL, 881, L11
Pecora, F., Servidio, S., Greco, A., & Matthaeus, W. H. 2021, A&A, 650, A20
Pecora, F., Servidio, S., Primavera, L., et al. 2023, ApJL, 945, L20
Perri, S., Pucci, F., Malara, F., & Zimbardo, G. 2019, SoPh, 294, 34
Perri, S., Valentini, F., Sorriso-Valvo, L., Reda, A., & Malara, F. 2017, P&SS, 140, 6
Pucci, F., Malara, F., Perri, S., et al. 2016, MNRAS, 459, 3395
Retinò, A., Khotyaintsev, Y., Le Contel, O., et al. 2022, ExA, 54, 427
Richardson, L. F. 1922, Weather Prediction by Numerical Process, II edn., Cambridge Mathematical Library (Cambridge: Cambridge Univ. Press)
Roberts, O. W., Alexandrova, O., Sorriso-Valvo, L., et al. 2022, JGRA, 127, e2021JA029483
Schwartz, S. J., Horbury, T., Owen, C., et al. 2009, ExA, 23, 1001
Servidio, S., Matthaeus, W. H., Shay, M. A., et al. 2010, PhPl, 17, 032315
She, Z.-S., & Leveque, E. 1994, PhRvL, 72, 336
Sorriso-Valvo, L., Carbone, V., Veltri, P., Consolini, G., & Bruno, R. 1999, GeoRL, 26, 1801
Spence, H. E. 2019, AGUFM, 2019, SH11B–04
Taylor, G. I. 1938, RSPSA, 164, 476
Tessein, J. A., Matthaeus, W. H., Wan, M., et al. 2013, ApJL, 776, L8
Tessein, J. A., Ruffolo, D., Matthaeus, W. H., & Wan, M. 2016, GeoRL, 43, 3620
Tessein, J. A., Ruffolo, D., Matthaeus, W. H., et al. 2015, ApJ, 812, 68
Valentini, F., Malara, F., Sorriso-Valvo, L., Bruno, R., & Primavera, L. 2019, ApJL, 881, L5
Veltri, P., & Mangeney, A. 1999, AIP Conf. Proc. 471 (Melville, NY: AIP), 543
Verscharen, D., Klein, K. G., & Maruca, B. A. 2019, LRSP, 16, 5
Vörös, Z., Jankovičová, D., & Kovács, P. 2002, NPGeo, 9, 149
Wan, M., Matthaeus, W. H., Karimabadi, H., et al. 2012, PhRvL, 1090000, 195001
Wan, M., Matthaeus, W. H., Roytershteyn, V., et al. 2016, PhPl, 23, 042307
Wan, M., Osman, K. T., Matthaeus, W. H., & Oughton, S. 2011, ApJ, 744, 171
Wang, L.-P., Chen, S., Brasseur, J. G., & Wyngaard, J. C. 1996, JFM, 309, 113